

Seismic reconstruction of seafloor sediment deformation during volcanic debris avalanche emplacement offshore Sakar, Papua New Guinea

Kühn, Michel; Karstens, Jens; Berndt, Christian; Watt, Sebastian

DOI:

[10.1016/j.margeo.2021.106563](https://doi.org/10.1016/j.margeo.2021.106563)

License:

Creative Commons: Attribution-NonCommercial-NoDerivs (CC BY-NC-ND)

Document Version

Peer reviewed version

Citation for published version (Harvard):

Kühn, M, Karstens, J, Berndt, C & Watt, S 2021, 'Seismic reconstruction of seafloor sediment deformation during volcanic debris avalanche emplacement offshore Sakar, Papua New Guinea', *Marine Geology*, vol. 439, 106563. <https://doi.org/10.1016/j.margeo.2021.106563>

[Link to publication on Research at Birmingham portal](#)

General rights

Unless a licence is specified above, all rights (including copyright and moral rights) in this document are retained by the authors and/or the copyright holders. The express permission of the copyright holder must be obtained for any use of this material other than for purposes permitted by law.

- Users may freely distribute the URL that is used to identify this publication.
- Users may download and/or print one copy of the publication from the University of Birmingham research portal for the purpose of private study or non-commercial research.
- User may use extracts from the document in line with the concept of 'fair dealing' under the Copyright, Designs and Patents Act 1988 (?)
- Users may not further distribute the material nor use it for the purposes of commercial gain.

Where a licence is displayed above, please note the terms and conditions of the licence govern your use of this document.

When citing, please reference the published version.

Take down policy

While the University of Birmingham exercises care and attention in making items available there are rare occasions when an item has been uploaded in error or has been deemed to be commercially or otherwise sensitive.

If you believe that this is the case for this document, please contact UBIRA@lists.bham.ac.uk providing details and we will remove access to the work immediately and investigate.

Seismic reconstruction of seafloor sediment deformation during volcanic debris avalanche emplacement offshore Sakar, Papua New Guinea

Michel Kühn^{1,2}, Jens Karstens¹, Christian Berndt¹, and Sebastian F. L. Watt³

mkuehn@geomar.de

¹GEOMAR Helmholtz Centre for Ocean Research Kiel, Wischhofstraße 1-3, 24148 Kiel, Germany

²Institute of Geosciences, Christian-Albrechts-Universität zu Kiel, Otto-Hahn-Platz 1, 24118 Kiel, Germany

³School of Geography, Earth and Environmental Sciences, University of Birmingham, Edgbaston, Birmingham, B15 2TT, United Kingdom

Abstract

Volcanic island sector-collapses have produced some of the most voluminous mass movements on Earth and have the potential to trigger devastating tsunamis. In the marine environment, landslide deposits offshore the flanks of volcanic islands often consist of a mixture of volcanic material and incorporated seafloor sediments. The interaction of the initial volcanic failure and the substrate can be highly complex and have an impact on both the total landslide deposit volume and its emplacement velocity, which are important parameters during tsunami generation and need to be correctly assessed in numerical landslide-tsunami simulations. Here, we present a 2D seismic analysis of two previously unknown, overlapping volcanic landslide deposits north-west of the island of Sakar (Papua New Guinea) in the Bismarck Sea. The deposits are separated by a package of well-stratified sediment. Despite both originating from the same source, with the same broad movement direction, and having similar deposit volumes ($\sim 15.5\text{-}26\text{ km}^3$), the interaction of these landslides with the seafloor is markedly different. High-resolution seismic reflection data show that the lower, older deposit comprises a proximal, chaotic, volcanic debris avalanche component and a distal, frontally confined component of deformed pre-existing well-bedded seafloor-sediment. We infer that deformation of the seafloor-sediment unit was caused by interaction of the initial volcanic debris avalanche with the substrate. The deformed sediment unit shows various compressional structures, including thrusting and folding, over a downslope distance of more than 20 km, generating >27 % of

shortening over a 5 km distance at the deposit's toe. The volume of the deformed sediments is almost the same as the driving debris avalanche deposit. In contrast, the upper, younger landslide deposit does not show evidence for substrate incorporation or deformation. Instead, the landslide is a structurally simpler deposit, formed by a debris avalanche that spread freely along the contemporaneous seafloor (i.e., the top boundary of the intervening sediment unit that now separates this younger landslide from the older deposit). Our observations show that the physical characteristics of the substrate on which a landslide is emplaced control the amount of seafloor incorporation, the potential for secondary seafloor failure, and the total landslide runout far more than the nature of the original slide material or other characteristics of the source region. Our results indicate the importance of accounting for substrate interaction when evaluating submarine landslide deposits, which is often only evident from internal imaging rather than surface morphological features. If substrate incorporation or deformation is extensive, then treating landslide deposits as a single entity substantially overestimates the volume of the initial failure, which is much more important for tsunami generation than secondary sediment failure.

Keywords: flank collapse, Bismarck Sea, landslide, volcano, tsunami, sediment failure

1. Introduction

In December 2018, a lateral collapse of the Indonesian volcano Anak Krakatau triggered a devastating tsunami, killing more than 400 people around the Sunda Strait. The initial collapse volume calculated at 0.2-0.3 km³, is relatively small in the context of volcano sector collapse (Siebert, 1984; Siebert and Roverato, 2021), but was still capable of generating a highly destructive tsunami (Gouhier and Paris, 2019; Grilli et al., 2019; Walter et al., 2019). In historic times, volcanic sector collapses have produced several devastating tsunamis, causing thousands of casualties around island-arc volcanoes (Auken et al., 2013; Day et al., 2015; Karstens et al.,

2019; Watt et al., 2021). The global frequency of historically documented tsunami-generating events is approximately 50-100 years (Day et al., 2015), including collapses at Oshima-Oshima, Japan, in 1741, Mt. Unzen, Japan, in 1792, Ritter Island, Papua New Guinea, in 1888, and Anak Krakatau in 2018 (Walter et al., 2019). This shows that volcanic flank failure and resultant tsunami genesis poses a serious natural hazard for coastal regions in volcanic settings worldwide.

The Bismarck Archipelago hosts several island-arc volcanoes, of which more than eleven have recognized offshore debris avalanche deposits (Silver et al., 2009), the product of past lateral collapses. The most recent and best studied of these is the 1888 Ritter Island collapse (Johnson et al., 1987; Silver et al., 2009; Ward and Day, 2003; Watt et al., 2019), which is also the largest volcanic sector collapse globally that has been recorded in historic times (Day et al., 2015). Recent studies show that the volume of the submarine landslide-derived deposit west of Ritter is 13 km³, but the initial tsunamigenic flank collapse that produced these deposits was only ~2.4 km³ (Karstens et al., 2019; Watt et al., 2019). This substantial difference in volume between the offshore deposits and the primary failure illustrates the potential complexity of landslide processes in volcanic-island settings, where the initial mass movement can lead to extensive substrate incorporation and secondary failure. Such complexities are not restricted to volcanic islands, but have also been recognized in submarine landslides in non-volcanic settings (e.g., Lenz et al., 2019; Morita et al., 2011; Ogata et al., 2019; Sobiesiak et al., 2018), and constitute an important general process in the emplacement of subaqueous landslide deposits. Past work at Ritter, as well as a survey of landslide deposits offshore Montserrat, Lesser Antilles (Crutchley et al., 2013; Watt et al., 2012a, 2012b), has also shown that both bathymetric and internal geophysical data (with further insights provided by direct sampling) are required to accurately reconstruct the complex sequence of transport and dynamics involved in landslide emplacement offshore volcanic islands. In particular, the internal architecture of deposits is key to revealing evidence of substrate incorporation, and for the estimation of the initial volume of

volcanic debris. The process of substrate incorporation as well as the decoupling of submarine landslides from the substrate, has also been extensively studied on exhumed ancient mass transport deposits onshore (Ogata et al., 2019; Sobiesiak et al., 2018). These studies show that substrate decoupling occurs where a lubricating layer between the landslide and the substrate prevents the transmission of shear stress from the flow into the substrate (Ogata et al., 2014b; Sobiesiak et al., 2018) and that substrate incorporation occurs where either the basal drag of the flow is great enough to plough the slide mass into the substrate, or where a dragged tool (e.g., a coherent slide block) is pressed into the substrate's surface at the base of the flow, ripping off substrate material (Sobiesiak et al., 2018).

During a marine geophysical survey on board RV SONNE (SO252), we surveyed the seafloor around Ritter and the neighboring islands of Sakar and Umboi (Fig. 1). Beside the deposits of the 1888 Ritter Island sector collapse, we identified two additional, buried landslide deposits west of Sakar that vary in extent and morphology. These differences relate to distinct patterns of seafloor interaction and internal structures. Understanding the transport and emplacement processes that lead to such deposits, and how and why the morphology and extent of deposits vary, is key to constraining tsunami magnitudes and providing hazard assessments for coastal regions potentially subject to volcanic-tsunami hazards (Løvholt et al., 2015).

The main aim of this paper is to identify the processes that resulted in the two different types of volcanic landslide deposit observed offshore Sakar, by targeting two objectives. The first objective is to determine the origin of the seismically imaged deposits. We use high-resolution 2D seismic data to reconstruct the geometry (extent and thickness) of the deposits to test whether they originated from Umboi, Sakar or Ritter. The second objective is to constrain the emplacement dynamics of the landslides with a focus on their interaction with the underlying substrate. We use seismic characteristics such as internal reflection patterns, amplitude variations, and the configuration of the top and bottom bounding reflectors to interpret the origin of different sub-facies within the landslide deposits and their relationship to each other,

thereby evaluating the extent of the primary failure mass and evidence of substrate incorporation and deformation.

2. Geological Background

2.1 Regional tectonics

Sakar is a volcanic island located on the southern margin of the Bismarck microplate, forming a part of the Western Bismarck volcanic arc (Fig. 1). This 1000 km-long volcanic arc extends onto the larger island of New Britain to the east, and arc volcanism in this setting is associated with the northward subduction of the Solomon microplate and of a relict slab further west, where the arc has collided with the New Guinea continental margin (Baldwin et al., 2012; Honza et al., 1989; Johnson et al., 1987; Taylor, 1979). This tectonically complex zone of microplates lies in a region of oblique convergence between the Pacific and Australian plates (Baldwin et al., 2012; Holm and Richards, 2013; Woodhead et al., 2010). The eastern and western ends of the Bismarck arc are cut by the Bismarck Sea Seismic Lineation, a seismically active series of left-lateral transform faults and spreading segments separating the South Bismarck plate and the North Bismarck plate (Baldwin et al., 2012; Taylor, 1979; Fig. 1).

2.2 Geology and Topography

Sakar is the northernmost of a group of three islands approximately 25 km west of New Britain, (Fig. 1). The larger volcanic island of Umboi is 15 km south of Sakar, and the much smaller island of Ritter – the subaerial remnant of the 1888 lateral collapse – lies in between. Rock samples show that the volcanism of the western Bismarck arc, including that on Ritter, Umboi and Sakar, is dominated by basaltic magmas (Johnson, 1977; Woodhead et al., 2010).

Sakar has a broadly symmetrical conical form, with gullied slopes that rise steeply to the island summit. The island diameter at sea level is approximately 8 km, but the entire structure rises from a base ~1500 m below the sea surface, with a diameter of ~25 km, to a maximum height

of ~900 m above sea level. The summit crater is approximately 1.5 km wide and contains a crater lake (Johnson et al., 1972). The island is formed by this single main volcanic edifice, which is dominated by porphyritic basaltic lavas, with subsidiary andesites. Around the island shoreline are volcanoclastic alluvial deposits, and there are parasitic volcanic cones in the northern part of the island (Johnson et al., 1972). No historical eruptions are known from Sakar, but several hot springs on the southwestern shore (Johnson et al., 1972), as well as its youthful morphology, suggest that it is potentially active. Offshore, the island is fringed by coral reefs. The seafloor offshore Sakar was surveyed in 2004 by the RV Kilo Moana, on a research expedition that mapped 12 landslide deposits in the Bismarck volcanic arc (Silver et al., 2009). This expedition investigated in detail the submarine deposits from the lateral collapse of Ritter in 1888 (Day et al., 2015; Johnson et al., 1987; Karstens et al., 2019; Silver et al., 2009; Ward and Day, 2003), which travelled between Sakar and Umboi and into the basin northwest of the islands. It also identified a field of hummocks north of Sakar – a different area from that described in this paper – and interpreted this to be the blocky facies of a debris avalanche deposit originating from Sakar. This deposit covers an area of 30 km² to a distance of more than 10 km from the island's coast (Fig. 2). The lack of a collapse scar was explained by later volcanic growth and the formation of coral reefs within the avalanche's source area. However, several irregular valleys at the flanks around Sakar indicate potential source areas of landslides (Fig. 2; Silver et al. 2009).

3. Data and Methods

During scientific cruise SO252 on R/V SONNE in November/December 2016, we collected 2D multichannel seismic data using a 250 m-long (160 channels) streamer system with a group spacing of 1.56 m [dataset](Berndt et al., 2021b). As the seismic source, we used two GI airguns, shot in harmonic mode (105/105 cubic inch). In total, we collected 680 km of seismic

reflection profiles (Fig. 1). The data were processed with a 10, 45, 250, 400 Hz bandpass filter, a normal moveout correction (constant velocity: 1495 m/s, derived from CTD measurements), and a post-stack 2D-stolt-migration using a constant velocity of 1500 m/s. The bathymetry of the survey area was mapped using two multibeam systems (Kongsberg EM710 and EM122) with a horizontal resolution of 25 m [dataset](Berndt et al., 2021a). For the maps shown in this study, we merged the acquired high-resolution bathymetry grid with a low-resolution global GEBCO grid. Detailed acquisition and processing descriptions can be found in the SO252 cruise report (Berndt et al., 2016).

The range of data collected on cruise SO252 also includes a 3D seismic dataset (Karstens et al., 2019), high-resolution sub-bottom echosounder profiles (Parasound P70 system) and high-resolution video sledge derived photography (Watt et al., 2019), as well as grab samples. To derive a 2D velocity model by forward modeling, six three-component ocean bottom seismometers (OBS) were deployed along a profile within the 3D seismic cube.

Depth, thickness, and volume calculations of sedimentary units mapped using the 2D seismic data were carried out with a seismic velocity of 1760 m/s, derived from OBS experiments (Karstens et al., 2019). Areas and volumes were determined by picking the top and base reflections of sedimentary units on cross-cutting seismic profiles. Relative shortening in units with resolvable compressional structures along the profiles was graphically estimated, using the ratio between the observed extent of the compressional zone and the length of mappable reflections within the seismic data along the deformed reflectors at zero vertical exaggeration. As parts of the compressional structures cannot be resolved properly in the seismic data, shortening values have to be considered minimum estimates. Absolute displacement values of thrust faults were calculated by dividing the picked horizontal distance of a thrust horizon overlying its undeformed counterpart by the cosine of the fault dip angle.

4. Results

4.1 Seismic facies

The stratigraphy northwest of Sakar and Ritter, and north of Umboi, was extensively imaged within the seismic data collected during cruise SO252, with examples shown in Figs. 3 and 4. The data reveal two generally different seismic facies: one defined by continuous and parallel reflections and a second one characterized by chaotic and rather transparent (i.e., lower amplitude) seismic reflections.

The dominant sub-seafloor facies consists of continuous and parallel reflections. This facies is typified by laterally coherent reflections with generally consistent amplitudes. The reflections appear relatively homogenous and are sub-horizontal, lacking any hummocky or steeply dipping morphological features, and representing the seismic image of well-bedded sediments. Subsequently we will refer to this facies as the well-bedded sediment facies.

The second facies, characterized by chaotic and relatively transparent reflections, occurs in two discrete and broadly horizontal packages, that interrupt the well-bedded sediment facies northwest of Sakar. We divide this chaotic facies into two types. The first type contains irregular surfaces with dipping, sometimes irregular or wavy top boundary reflections. This sub-facies has top and bottom boundaries with high seismic amplitudes, while it is internally chaotic, with most parts being significantly more transparent than the well-bedded sediment facies. This internally chaotic sub-facies is present in two distinct packages of reflections on and near the western flank of Sakar. We consider these packages to represent landslide deposits: a shallow deposit subsequently referred to as Sakar Landslide Deposit 1 (SLD1) and a deeper deposit referred to as Sakar Landslide Deposit 2 (SLD2), which we describe in detail within the following subsections. The second chaotic sub-facies is relatively transparent, too, but contains internal reflections that are parallel-bedded and mostly continuous. This sub-facies occurs as a distal continuation of the internally chaotic sub-facies in SLD2. We interpret its characteristics

as corresponding to deformed bedded sediments, forming the outer part of SLD2, and will subsequently refer to this as the deformed sediment sub-facies.

4.2 Seafloor morphology

The submarine morphology northwest of Sakar is dominated by a sub-circular field of randomly distributed hummocks (i.e., positive, relatively steep-sided bathymetric features encircled by a clear break in slope), covering an area of 240 km² with long-axis diameters >100 m (Fig. 2). This hummock field is separated from that previously identified north of Sakar by Silver et al. (2009), and partially overlaps with the distal part of the transport path of the 1888 Ritter Island landslide deposits (Fig. 2; Day et al., 2015; Watt et al., 2019). Within the hummock field northwest of Sakar, 92 hummocks have maximum diameters between 100 and 500 m (at the basal break in slope), 23 between 500 and 1,000 m and two between 1,000 and 1,100 m, covering individual surface areas between ~0.05 km² and ~1.21 km². The second largest hummock was transected by two seismic profiles (Fig. 3A, C), and covers a surface area of ~1 km² with a height > 80 m above the surrounding seafloor. The flanks of this hummock continue down to 120 m below the seafloor and are resolvable to the center of SLD2 (internally chaotic sub-facies) (Fig. 3). In contrast, the basal reflection of SLD1 continues below most of the other, smaller hummocks that are transected by seismic profiles, but is bent upwards, which we attribute to seismic velocity pull-up. Most of the hummocks observable at the present-day seafloor therefore appear to be rooted within SLD1 (Fig. 3B), and are partially buried by overlying sediment. Some hummocks show an internal seismic stratification that is not parallel to the surrounding stratigraphy (Figs. 3B, C), while some show chaotic internal reflections (Fig. 3C) and others show no visible internal reflections (Fig. 3B), which is most likely a problem of seismic imaging. None of these hummocks has a conical shape, comparable to the conic landforms northwest of Ritter and south of Sakar (Karstens et al., 2019); instead, they appear

elongated and sub-angular, but without a preferred orientation. Their broad form is similar to volcanic landslide blocks in other offshore settings, such as those offshore Montserrat (Watt et al., 2012b) or El Hierro, Canary Islands (Masson et al., 2002), or in many subaerial volcanic settings (e.g., Yoshida et al., 2012). The average slope between the hummocks dips 2.5° seaward close to Sakar and $< 0.5^{\circ}$ at the north-western limits of the hummock field. Outside of the hummocky field the seafloor is generally smooth and flat (Fig. 2) with an overall slope gradient below 0.5° . However, there are areas within the field containing parallel ridges trending southeast-northwest (Fig. 2) with wavelengths of ~ 200 m and amplitudes of ~ 5 m; and a relatively small field of elongated seafloor depressions with diameters between 200 and 500 m and 5 to 15 m depth. Northwest of the hummock field the seafloor morphology is dominated by several smooth-surfaced lobes, interpreted as the distal deposits of the 1888 Ritter Island collapse (Watt et al., 2019).

Our bathymetric data show that the field of hummocks north of Sakar (cf. Silver et al., 2009) has block sizes and distribution similar to those in the north-western field mapped here. As there are no seismic data imaging the subsurface of the second hummock field to the north, and because it is separated from the one mapped here by several kilometers, we do not further investigate the area north of Sakar within this paper.

4.3 Landslide deposit stratigraphy

4.3.1 Sakar Landslide Deposit 1 stratigraphy

Directly below the seafloor reflection west of Sakar, a ~ 10 m-thick unit with chaotic internal reflections is located (Fig. 3A, 4). Watt et al. (2019) interpreted it to be the deposit of the 1888 Ritter Island sector collapse. The Ritter deposit overlies a ~ 50 m-thick package of well-stratified reflections (Fig. 4), but to the east, closer towards the slope of Sakar, it overlies SLD1. In 2D profiles, the latter forms a tapering, wedge-shaped deposit, seismically characterized by the internally chaotic sub-facies, with an average thickness of 67 m (Figs. 3, 4). SLD1 can be

correlated across multiple profiles, defining a laterally fan-shaped deposit (Fig. 1) extending over an area of $\sim 250 \text{ km}^2$ with a volume of $\sim 15.5 \text{ km}^3$. Close to the flank of Sakar, the boundary between SLD1 and the underlying bedded stratigraphy, which has an increasingly chaotic general appearance in seismic reflection profiles, becomes obscure (Fig. 4A). Although the general seismic appearance of SLD1 corresponds to the internally chaotic sub-facies, at least two continuous internal reflections can be traced over a distance of 1 km, with a seismic waveform that consists of one peak overlying one trough.

SLD1 is thickest on the slope of Sakar (slope gradient 2.5°), tapering to the west. In this area, its top boundary reflection is indistinguishable from the seafloor reflection, which has a hummocky seismic appearance. The lateral margins of SLD1 as well as the area where its upper surface is indistinguishable from the seafloor (on the outer flank of Sakar), correlate with the margins of the hummock field northwest of Sakar observed in the bathymetry (Fig. 2). The volume stated above includes the hummocks intersected by the seismic data that appear to be rooted within SLD1; hummocks between and off the seismic profiles, as well as the large block shown in Fig. 3A, which appears to be rooted within SLD2, are not included. Due to the limited coverage of the 2D seismic lines, the extent of SLD1 could not be mapped entirely. Extent and volume thus have to be considered minimum values.

4.3.2. Sakar Landslide Deposit 2 stratigraphy

At a depth of 60 – 70 m below the seafloor, the top boundary of SLD2 extends over an area of 590 km^2 (Fig. 1) and has an elongated shape. The average thickness of the deposit is 71 m, which remains relatively consistent over the entire extent. Deposit thickness tapers to less than 60 m at the north-eastern and south-western margins. We divide the deposit into three parts: A proximal part close to Sakar, seismically characterized by the internally chaotic sub-facies (similar to SLD1); a middle part, characterized by the deformed sediment sub-facies; and a distal toe consisting of the deformed sediment sub-facies as well, but with more coherent

284 reflections that show extensively folded and thrust-faulted reflections (Fig. 4B). All three parts
285 are included in the volume and extent values stated here.

286 In the southeasternmost part of the seismic profile in Fig. 4, the proximal part of SLD2 is
287 separated from SLD1 by a continuous reflection package of ~15 m maximum thickness over a
288 downslope distance of ~3 km. Close to the outer flank of Sakar, seismic reflections are generally
289 chaotic, and amplitudes decrease with time in respect to depth more strongly than in the basin
290 west of the island. Because of this, it is very difficult to distinguish the bottom boundary of the
291 internally chaotic sub-facies in SLD2. For this study, we chose the first continuous high-
292 amplitude reflection to define the base of SLD2 in this area, but the true boundary may be
293 located even deeper. Therefore, we consider the volume of this part of SLD2, of 12.5 km³, as a
294 minimum volume. The depth of the continuous basal reflection varies within +/- 10 m, resulting
295 in a proximal deposit thickness of 47 m to 61 m (Fig. 4). Within the seismic data the surface of
296 the proximal SLD2 has an apparent downslope angle between 0.5 and 2.0 °, following the
297 general slope trend close to Sakar.

298 The downslope limit of the proximal part of SLD2 coincides with the appearance of more
299 continuous internal reflections (the transition from the internally chaotic to the deformed
300 sediment sub-facies), a basal upward step of the deposit's bottom boundary reflection, and a
301 break in the slope gradient. This defines the start of the middle part of SLD2. Internally, the
302 reflections in this part of SLD2 have lower amplitudes than the bounding stratigraphy but show
303 visible continuity over ~ 17 km distance. This continuity is only disrupted by vertical seismic
304 anomalies of upward bent reflections (Fig. 4B). Across the transition from the proximal to the
305 middle part of SLD2, the top reflections are undulated, over a distance of more than 5 km (Fig.
306 4B). This upper surface morphology consists of seven undulations with wavelengths between
307 500 m and 1300 m and amplitudes between 3 m and > 8 m. These transition, to the northwest
308 into reflections concordant to the well-bedded sediment facies above (Fig. 4B). Directly below
309 the top reflection, a ~10 m thick package of continuous reflections with higher coherency than

the internal reflections below is resolvable, until it is cut by the deformation marking the start of the distal toe of the deposit (Fig. 4B). The upper surface of SLD2 transitions from a (apparent) north-western dip of 0.16° to an (apparent) south-eastern dip of 0.17° towards the deposit's toe. The bottom boundary reflection steps upwards from the proximal part of SLD2, becoming shallower by ~ 23 m over a downslope distance of ~ 1000 m. This marks the bottom boundary-limit between the internally chaotic sub-facies in the proximal part and the deformed sediment sub-facies in the middle part of SLD2. Beyond this step, the basal reflection is generally continuous and concordant with the underlying stratigraphy, and its amplitude decreases towards the distal part of SLD2.

The distal part of SLD2 is dominated by thrusting and folding. The boundary between the middle and distal part is characterized by the appearance of higher-amplitude internal reflections, in which compressional structures become clearly visible. At least five thrust faults can be identified over a downslope distance of more than 5 km, with fault dip angles between 12° and 17° and an apparent southeast dip direction, parallel to the profile direction (Fig. 5C). Between the thrusts and folds, the seismic reflections are irregularly deformed, with a chaotic appearance and without resolvable faulting or folding. Due to this chaotic nature, absolute displacement calculations were only possible for two of the thrust faults, giving individual displacement values of 73 m and 82 m (± 20 m picking uncertainty due to the chaotic seismic character). From relative graphical estimations (see 3. Data and Methods) a horizontal shortening of 27% caused by thrusting and folding is estimated over the most distal 5 km of the toe region (in the direction of the seismic profile; Fig. 5C).

The deformation of both the middle and distal part of SLD2 occurs on the same basal reflection and suggests that this represents the primary shear surface. The reflections directly below this basal shear surface are coherent, but within the first 25 ms-interval they are more transparent than deeper reflections, with evidence for some disturbance (Fig. 4B), suggesting a narrow zone of additional shear, decreasing downwards, and terminating at the base of this 25 ms interval.

Below the distal toe region, reflections are truncated by a series of apparently northeast and southeast dipping normal faults (Fig. 4B). The middle and distal part of SLD2, all comprising the deformed sediment sub-facies, have a volume of $\sim 13.5 \text{ km}^3$.

5. Discussion

5.1 Origin and emplacement of SLD1

SLD1 is characterized by a fan-shaped hummocky topography and its seismic character corresponds to the internally chaotic sub-facies. Hummocky topographies around many volcanoes globally are representative of the blocky facies of debris avalanche deposits (e.g. Mount St Helens, Glicken 1996), although broadly comparable topographies may also be formed by scattered volcanic vents and cones (e.g. Azores, Weiß et al. 2015), or by erosional processes (e.g. Ritter Island, Karstens et al. 2019). Internal reflections indicate stratification within the hummocks of SLD1, and these can be used as an indicator of their origin. Reflections parallel to the underlying stratigraphy would be expected if the hummocks are the result of erosion, while conical forms, with reflections parallel to the flanks of the hummock or with broken, upward-bended reflections at the base of the hummock, would be typical for volcanic cones (both examples can be found west of Ritter; Karstens et al., 2019). However, most of the hummocks off Sakar lack internal stratification or have internal reflections with a dip that is discordant with that of the surrounding stratigraphy. They also have irregular, sub-angular shapes, steep sides and in some cases relatively flat tops. Together, these observations suggest that the hummocks represent transported blocks. Due to the fan-shaped distribution of these blocks at the foot of Sakar we interpret them as being from a common source and emplaced in a single mass movement, and that they thus represent the blocky facies of a debris avalanche deposit. The random distribution of these blocks within the fan is indicative of a freely spreading avalanche (Yoshida et al., 2012). This implies that the flow velocity in the

emplacement direction was not significantly higher than the flow-perpendicular spreading velocity (Crutchley et al., 2013).

The areal extent of the northwestern block field in the bathymetric data matches the seismic extent of SLD1, except in the northwesternmost part of the profiles, where the burial depth of SLD1 is too deep for blocks to protrude at the seafloor. This indicates that the bathymetric expression can be used to constrain the minimum extent of the blocky part of the debris avalanche but does not resolve the margins of the shallowly buried deposit. The high seismic amplitude of the boundary reflections is indicative of a significant change in seismic impedance, implying a different nature of the deposited material within and around SLD1. Seismic reflections within SLD1 are generally discontinuous, chaotic, and transparent. However, there are some coherent reflections extending laterally up to 1000 m. These suggest that the deposit was not emplaced as a simple, fully disaggregated one-directional flow or avalanche. The reflections may either indicate deposition in separate stages or phases of one major event, representing the interface between different flow lobes or pulses (e.g., Deposit 1, Montserrat, Crutchley et al., 2013; Lebas et al., 2011), or they may correspond to a thin (i.e., sub-seismic) unit of hemi-pelagic sediments indicating a period of normal sedimentation between unrelated flank collapse events. As these reflections are not visible on all seismic lines that image the deposit and are laterally restricted, we consider the first scenario more likely.

Due to the geometry and location of SLD1, the debris avalanche most likely originated from Sakar. There are multiple morphological structures that may reflect the scars of past sector collapses onshore Sakar Island (Silver et al., 2009). However, none of them correlates spatially with the deposit, and it is ambiguous if they have large enough dimensions to be the source of a $>10 \text{ km}^3$ landslide deposit, suggesting that younger volcanic activity has entirely overprinted the onshore part of the SLD1 collapse scarp.

The hummocky proximal morphology of SLD1, in combination with its fan-shaped extent and chaotic internal structure, unequivocally shows that it is a submarine landslide deposit (Frey-

Martínez et al., 2006). Similar deposits with volcanic origin have been identified in many locations (Watt et al., 2021) including Montserrat (Deposit 1; Watt et al. 2012b, a; Crutchley et al. 2013; Karstens et al. 2013) and Fogo, Cape Verde (Day et al., 1999; Le Bas et al., 2007; Masson et al., 2008). The fan shape of the deposit suggests a cohesionless flow dominated by energy dissipation through granular particle interactions, which is typical for freely-spreading heterogenous and generally coarse-grained volcanic debris avalanches (Mulder and Cochonat, 1996; Watt et al., 2012a, Watt et al., 2021).

Within SLD1, there is no seismic or bathymetric evidence for the secondary incorporation of underlying material (including that of SLD2). According to Sobiesiak et al. (2018), a decoupling of the sliding mass from the substrate, “free-slip flow”, occurs where shear stress transmission from the flow into the substrate is prevented by a lubricating layer. The study suggests the formation of this lubricating layer by one (or a combination) of the following mechanisms: hydroplaning, shear wetting, and/or liquefaction. During hydroplaning the hydrodynamic water pressure at the flow front increases and is transferred into the underlying bed, forming a water-rich sediment layer between flow and substrate (Mohrig et al., 1998). Shear wetting describes the generation of a soft, diluted, lubricating layer due to high shear rates between the water and the sediment boundary during flow (De Blasio et al., 2005). Ogata et al. (2014a) describe liquefaction of poorly consolidated sands where the induced shear of the flow causes a loss of grain contacts within the sand layers. As the flow stops, these liquified sands inject upwards into the basal flow deposit. Our seismic data do not provide the resolution to allow us to distinguish between these different processes (such as the observation of basal injections of sand (e.g. vertical fluid escape structures), which would be indicative for liquefaction (Ogata et al., 2014a, 2012), and while we cannot provide further constraints, we consider it likely that one or a combination of these processes led to a decoupling of the SLD1 debris avalanche and the contemporaneous seafloor.

Southwest-northeast trending ridges within the hummock field and north of Sakar (Fig. 2) are most likely related to later sedimentary processes, e.g., sediment waves (Pope et al., 2018). They also could be related to the deposition of the 1888 Ritter Island collapse debris flow (Watt et al. 2019), but in either case, we do not interpret them as being directly associated with SLD1. As the Ritter Island 1888 deposits partially overlap with the SLD1 hummock field (Fig. 2), we cannot exclude some erosion of SLD1 by the Ritter Island debris flow, although the burial depth of SLD1 in most places is deeper than the bottom boundary of the Ritter Island, and any erosion is thus not likely to have had a major impact on the morphology or our estimated volume of SLD1.

5.2 Origin and emplacement of SLD2

SLD2 extends from the outer flank of Sakar 30 km into the neighboring basin northwest of Sakar and Umboi (Fig. 1). Based on its location and its shape, an origin from Umboi, Sakar or Ritter may be possible. However, an origin from the relatively small edifice of Ritter is unlikely due to the large volume of the proximal component (12.5 km³) and because the deposit lies partly on the flanks of Sakar, which would require an element of upslope, northward bending transport and deposition. The shape and thinning pattern are most consistent with a landslide originating from the western slope of Sakar. This agrees with the direction of deformation patterns in the outer parts of SLD2, indicating northwestward compressional deformation in the toe domain (Fig. 5).

The proximal part of SLD2 is seismically characterized by the internally chaotic sub-facies (Fig. 4). This is similar to the overall seismic image of SLD1, suggesting that this part of the deposit originated as a volcanic debris avalanche, similar to SLD1. The apparent rooting of a large, transported block that protrudes from SLD2 to the seafloor (Fig. 3A, C) supports this interpretation, and it is likely that the surface of SLD2 contained many such blocks or hummocks, the majority of which are now buried and no longer evident at the seafloor. The

outer margin of the internally chaotic sub-facies shows a direct lateral transition into the deformed sediment sub-facies (Fig. 4B). Hence, SLD2 shows characteristics typical for volcanic debris avalanches off volcanic islands, but at the same time its middle and distal part comprise large volume of deformed pre-existing sediments, and SLD2 thus represents a composite deposit of volcanic material and seafloor sediments.

As described above, the middle part of SLD2 contains a discrete unit in its uppermost part (Fig. 4B), which may indicate the deposit of an overrunning flow. This unit has an undulated upper surface, and although this morphology could be a result of later sedimentary processes, its seismic image is markedly different from bedforms typically associated with sediment waves, (Pope et al., 2018), and we interpret this undulating form to be a primary characteristic of the upper surface of SLD2.

The transition from a proximal debris avalanche deposit to deformed seafloor sediments (marked by basal step, Fig. 4B) suggests that SLD2 originated as a debris avalanche from Sakar that incised into the substrate, as shown by the lateral transition between the internally chaotic sub-facies and the deformed sediment beyond. This transition indicates that some seafloor sediment must be incorporated within the proximal, internally chaotic part of SLD2, unless this pre-existing sediment was entirely evacuated from this area. Beyond the proximal part of SLD2, some evacuated sediment, or a more mobile part of the driving debris avalanche, may have overran the pre-existing seafloor, giving rise to the discrete uppermost unit in the middle part of SLD2. This overrunning flow may have facilitated the downslope-propagating deformation of the underlying seafloor sediment (i.e., the deformed sediment sub-facies of SLD2), which formed beyond the front of the driving debris avalanche (e.g., see processes discussed in Watt et al., 2012b) (Fig. 6). This seafloor sediment package shows strong evidence of in-situ compressional deformation, particularly at its toe, but was not evacuated, defining a frontally confined mass transport deposit (Frey-Martínez et al., 2006). Beyond the limits of the frontally confined margin (Fig. 4B), we cannot find seismic indications for further mass transport,

although it is possible that the thin, distal parts of an overrunning flow are not resolvable within our seismic data.

The seismic analyses of debris avalanche deposits offshore Montserrat revealed composite deposits consisting of a volcanic subunit and a subunit of deformed and mobilized seafloor sediments (Deposits 2 and 8, Watt et al. 2012b, a; Crutchley et al. 2013), similar to SLD2. These composite deposits formed as the result of the collision of a volcanic debris avalanche with seafloor sediments, resulting in their mobilization and deformation. This interpretation was confirmed by IODP expedition 340 (Le Friant, 2015), which revealed the absence of volcanic debris avalanche deposits within the seismically transparent, distal subunit of Montserrat Deposit 2 and of comparable deposits offshore Martinique. The processes involved in the interaction between volcanic debris avalanches and underlying seafloor sediments are complex and there are various potential mobilization mechanisms (Watt et al. 2012b; Le Friant 2015).

Studies on exhumed ancient mass transport deposits onshore confirm the potential composite nature of landslide deposits. “Megabreccia” deposits in the Paleogene Friuli Basin (Italy/Slovenia) were interpreted as the result of bipartite slide masses with a lower cohesive blocky flow and an upper turbulent flow, deeply eroding into and deforming the substrate (Ogata et al., 2014b). Sobiesiak et al. (2018) discuss substrate incorporation mechanisms such as that driven by a basal drag of the flow mass great enough for it to erode into the substrate, ripping off the latter and incorporating it into the flow. Alternatively, similar effects may occur by the dragging of a tool (e.g., a transported block) pressed against the substrate and ripping it off, or by peel-back, where the substrate is pushed along a basal weak layer laterally bounded by sub-vertical shear zones. Ogata et al. (2019) suggest similar substrate incorporation processes such as the erosion of positive paleobathymetric highs, and the transfer of inertial stress of a moving flow into the substrate due to an abrupt change of the slope angle, where the momentum of well-lithified blocks is transferred into the substrate as the slide comes to rest.

Large blocks such as that imaged in Fig. 3A could potentially have functioned as tools, eroding the slide mass into the substrate where the gradient of Sakar's slope decreases. However, due to the limited resolution of our seismic data we cannot identify if one of the specific mechanisms outlined above represented the dominant mode of substrate erosion by the SLD2 debris avalanche.

The deformation pattern in the outer region of SLD2 is typical for the deposits of frontally confined landslides (Frey-Martínez et al., 2006) and has been observed in non-volcanic submarine mass-movements (e.g., Oregon, USA, Lenz et al., 2019; Shimokita peninsula, northeast Japan, Morita et al., 2011) as well as volcanic settings (e.g., Deposit 8 offshore Montserrat, Watt et al., 2012b). Substrate deformation as the result of the emplacement of volcanic debris avalanches has been seismically documented offshore Montserrat (Crutchley et al., 2013; Watt et al., 2012b, 2012a) and at Ritter Island (Karstens et al., 2019; Watt et al., 2019), where deformed and incorporated sediments contribute 80% of the total slide volume. Potential factors that define the absolute limit of deformation at the toe of SLD2 could be the reversal of the slope direction, adding gravitational forces to the shear resistance of the sediments against progressive shear failure of the deforming sediments as well as a topographic effect caused by several normal faults cutting through the strata below (Fig. 4B).

For the deformation of the well-bedded sediment sub-facies of SLD2, we favor a combined substrate deformation model, as follow (Fig. 6): Substrate incorporation (i.e., physical mixing of the volcanic debris avalanche with seafloor sediments) did not reach beyond the basal step that marks the foot of the internally chaotic sub-facies of SLD2. This coincides with a break in the slope gradient, (Fig. 4). The initial loading that triggered frontal deformation beyond this point could have been the result of a transfer of the blocky debris avalanche's momentum as it decelerated into the substrate, progressively increasing the shear stress on the sediment, causing disaggregation, deformation, and compression. Added to this, an overrunning flow may have facilitated propagation of deformation in the underlying sediment, but the potential mechanisms

of this process remain ambiguous. An overrunning flow could potentially liquify underlying sediments by increasing the pore pressure due to grain reorganization during shearing (Hornbach et al., 2015; Ogata et al., 2014a) similar to the shear failure of sensitive clay deposits onshore (Bjerrum, 1955; Quinn et al., 2012). With the vertical seismic anomalies in the middle SLD2 (Fig. 4B), we find indications for fluid migration pathways (Gee et al., 2007) which could represent liquefaction. However, we cannot rule out that these structures represent seismic imaging artifacts. A mechanism of shear coupling, as proposed for paleo-landslide deposits in the Karoo Basin, South Africa (Van Der Merwe et al., 2011) and discussed for Deposit 8 off Montserrat (Watt et al., 2012b), where the motion of an overrunning flow exerts forces on the underlying strata leading to deformation, appears less plausible for SLD2. Seismic evidence for an overrunning flow is only visible in the middle part of SLD2, whereas if this flow was the main agent of deformation via shear coupling, we would expect it to be present over the entire deposit, an alternative model that could explain the seafloor sediment beyond the margin of SLD2 could be that the younger emplacement of SLD1 loaded the older deposits, and triggered failure downslope of these via the shear failure mechanisms described above. Similar secondary seafloor mobilization and deformation of deeper sediment packages, including thrust faulting and folding, has been observed for non-volcanic landslides, e.g. offshore Oregon, where a series of slide blocks have caused deformation and horizontal compaction of underlying sediments within a 10 km area (Lenz et al., 2019). However, because the sediment failure in SLD2 is confined to a package that coincides with both the upper and lower boundaries of its proximal part, and does not affect younger sediment, a role for SLD1 in this process would only make sense if there was no time gap between SLD1 and SLD2. This is not the case, because we observe a package of sediment, partly onlapping on the top boundary of SLD2, that separates the two landslides (Fig. 4B).

A further possible model is that both SLD1 and SLD2 are part of one multistage sector collapse, whereby the deeper unit slowly crept downslope (forming SLD2), until the slope stability

reached a critical point and the shallower flank failed, resulting in a collapse that emplaced SLD1. This type of process was postulated by Karstens *et al.* 2019 for the 1888 sector collapse of Ritter Island. Such slow, deep-seated deformations are known from other volcanoes, e.g. Mt. Etna, Sicily (Urlaub *et al.*, 2018). Again, the similar proximal characteristics of SLD1 and SLD2, and the observation of reflections separating the two deposits, indicates a time gap between them that implies they are entirely separate lateral collapses. This does not preclude that the emplacement of both debris avalanches could have been preceded by prolonged gradual deformation at the base of Sakar's flanks that promoted instability, comparable to processes at Ritter Island (Karstens *et al.*, 2019) and around other volcanoes.

The base of SLD2 is defined by a mostly continuous, high-amplitude reflection representing a basal shear surface for the deformation of the sediment package above. However, below this reflection, the well-stratified sediments appear more transparent than further below (Fig. 4). A second strong reflection about 25 ms TWT below may represent another, secondary basal shear surface. This second reflection correlates vertically with the depth of the proximal chaotic part of the unit. As the reflections between both surfaces are weak and transparent, but not deformed, this may represent a zone of deeper, distributed deformation, less extensive than that within SLD2 above. The development of a basal shear zone, with different layers of shearing, rather than one single basal shear surface has been described on onshore exhumed mass transport deposits (Ogata *et al.*, 2014a; Sobiesiak *et al.*, 2018). The seismic data are inconclusive in indicating if this basal shear zone involved shear of the sedimentary strata, or just mobilization of pore fluids.

5.3 Dissimilarity of two landslide deposits from Sakar

The results described here show that Sakar has produced at least two voluminous debris avalanches, deposited on the western submerged island slope and the basin floor to the northwest. Because both debris avalanches are the result of sector collapse (i.e., they have

mobilized large parts of the flank of the same island) it may be expected that they have a similar composition and that their dynamic evolution was similar. However, while SLD1 appears to consist completely of volcanic debris avalanche material, only the proximal part of SLD2 hosts a debris avalanche component. The middle and distal parts of the deposit consist of deformed seafloor sediments. The volumes of SLD1 and the proximal, internally chaotic sub-facies of SLD2 are nearly equal. However, the entire SLD2, when including the deformed-sediment facies, has twice the volume of SLD1. The fan-shape of SLD1, indicating free-spreading of a cohesionless flow, contrasts with the elongated shape of SLD2, indicating a concentration of forces in one primary direction, equivalent to the direction of mass movement during the initial stage of a debris avalanche. The proximal part of SLD2 most likely eroded into and partly overran the substrate (coupling of flow and substrate), causing deformation in the frontal direction, while the seismically imageable part of SLD1 spread along and above the pre-existing seafloor (decoupling of flow and substrate).

Seismic interpretations of marine landslide deposits off volcanic islands in the Lesser Antilles have shown that debris avalanches can incorporate large volumes of substrate during transport (Deplus et al., 2001; Le Friant et al., 2003; Watt et al., 2012b, 2012a). In a most basic sense, the process of substrate incorporation into moving debris is an energy exchange between the flowing debris mass and the initially static seafloor sediments, where kinetic energy of the flowing mass is consumed to put the static mass in motion. The required amount of energy depends on the stability of the seafloor sediments, which is controlled by the slope gradient and the thickness of the sediment layer (Mangeney et al., 2010), but also by the type of the substrate material and its shear strength. The two deposits examined in this study differ in the nature of their substrate: the continuation of the sedimentary well-bedded seismic facies underneath the proximal part of SLD2 (albeit poorly imaged) suggests that it was deposited on relatively fine-grained and water-saturated seafloor sediment (i.e., typical basin-infilling sediment), that typically has a low shear resistance. This would have promoted incorporation and a proximal

incision of the debris avalanche mass into the substrata. In contrast, the base of SLD1 coincides with a package of chaotic reflections on the flanks of Sakar, separating it from the proximal part of SLD2, and in some profiles corresponds directly with the upper part of SLD2. We interpret this substrate as likely comprising coarse-grained, heterogenous volcanic material derived from the flanks of Sakar, which would be much harder to mobilize than the hemipelagic seafloor sediments of the basin floor (Karstens et al., 2013) – the sediment type on which SLD2 was emplaced. Because of this, SLD1 slid decoupled from its base. Landslide deposits are considered to generally have a higher resistance to being eroded and incorporated into overflowing landslide masses (Alves and Lourenço, 2010). Outcrop-oriented studies on sedimentary mélanges link different mechanisms of substrate incorporation not only to the physiographic setting, but also to different lithological characteristics of the associated mass transport deposits (Ogata et al., 2019). Combined with our interpretations of SLD1 and SLD2, this suggests that the substrate is a major control on the incorporation of seafloor sediment by a debris avalanche. The difference in the nature of the substrate from water-saturated, homogenous seafloor sediments below SLD2 and a denser and more heterogenous volcanoclastic substrate below SLD1, minimized the substrate incorporation and kinetic energy loss in SLD1. This led not only to a smaller total volume of SLD1 but also to a longer runout compared to the debris avalanche component of SLD2.

5.4 Tsunami hazard

Landslides are the second most common trigger for tsunamis (Harbitz et al 2014) and have received increased attention with the 2018 Anak Krakatau flank collapse (Grilli et al., 2019). Numerical tsunami simulations of this event were conducted assuming a volume of initially 0.22 – 0.3 km³ of volcanic material, which was inferred from pre- and post-collapse aerial and satellite imagery and produced results that were consistent with the observed wave characteristics and run-up heights (Grilli et al., 2019). However, numerical landslide tsunami

simulations rely heavily on the applied input parameters. In case of submarine landslides, the most important tsunami source parameters are the slide volume and its emplacement velocity (Løvholt et al., 2005), which are only poorly constrained for most historic events (with Ritter Island being a rare exception). Instead, volume estimations are often based on acoustic imaging data of flank collapse deposits, such as bathymetric and seismic data. Our results on SLD2 as well as those from Montserrat and Ritter (Karstens et al., 2019; Watt et al., 2012a) show that estimating the volume of the initial volcanic debris avalanche only from the surface area of a landslide deposit and the thickness of a stratigraphic unit can be misleading. Without high-resolution seismic data, SLD2 could be easily misinterpreted as one unit of chaotic reflections that resulted from a single-event debris avalanche. The actual volume of the debris avalanche component in SLD2 is less than half that of the complete stratigraphic unit, while the remainder consists of deformed or mobilized seafloor sediments. This underlines the necessity of high-resolution seismic data for accurate volume estimations and tsunami modelling constraints.

The second important constraint in tsunami modelling is the emplacement velocity, which is likely heavily influenced by interaction of the slide mass and the substrate causing a transfer of kinetic energy. A more rapid deceleration of the sliding mass (if occurring in water depths relevant for tsunami genesis) would reduce the magnitude of the resulting tsunami, while the effect of substrate incorporation (increasing the water column) has little impact compared to the initial volcanic flank component. Numerical tsunami simulations of the 1888 Ritter Island sector collapse suggest that tsunami generation was primarily controlled by the collapse of the volcano, i.e. the initial failure volume and acceleration, and that deeper seated deformation and seafloor sediment incorporation had no significant effect on the tsunami amplitude (Karstens et al., 2020). This is in agreement with tsunami potential calculations for landslide deposits off Montserrat, which have shown that tsunami amplitudes for submarine sediment failures with an associated low height drop are an order of magnitude smaller than flank collapse-related tsunami amplitudes of the same volume (Watt et al., 2012a). Hence, it is unlikely that the

seafloor sediment failure and deformation imaged in the middle and distal parts of SLD2 affected the tsunami amplitude significantly, although they may result in longer wavelengths, as shown by a tsunami model for Deposit 2 off Montserrat (Watt et al., 2012a). Our analysis reveals once again that the complexity of volcanic sector collapse and debris avalanche emplacement in island settings, and highlights that tsunami hazard assessment for this comparably common process is still lacking reliable constraints for the most important source parameters.

6. Conclusions

The slope west of Sakar hosts two previously unknown landslide deposits. The younger deposit, SLD1, comprises volcanic debris avalanche material from Sakar, whereas the deeper SLD2 is a combination of a primary debris avalanche deposit and deformed and incorporated substrate. The toe domain of SLD2, which hosts folded and thrust-faulted sediments was shortened by at least 27 %. We suggest that the debris avalanche component of SLD2 partly eroded into and overran the substrate and triggered a progressive, lateral increase of the sediment pore pressure, resulting in a decrease of shear strength in the direction of the initial mass movement and mobilization and deformation of the pre-slide subsurface stratigraphy. We propose that the nature of the slide plane substrate is the most important control on sediment mobilization and secondary failures, and that this determined the different sizes and evolution of the two landslide deposits west of Sakar, which originated from the same source and were deposited on the same slope.

The main controlling parameters of landslide-generated tsunami amplitudes are the initial volume of the sliding mass that interacts with the ocean and its further acceleration. Estimating the initial volume of a flank or sector collapse by calculating the volume of the associated

landslide deposits involves a significant uncertainty. For SLD2 there is evidence that less than half of the landslide deposit's volume can be assigned to the initial debris avalanche.

7. Acknowledgements

We thank the master and the crew of the RV SONNE for their support during research cruise SO252. We also thank Dr. Ingo Klaucke and Dr. Christoph Böttner for the onboard-processing of the bathymetry data. We acknowledge Kei Ogata, Fabiano Gamberi and Derek Sawyer for improving the quality of the manuscript with their reviews. We would like to thank the GEBCO initiative for providing access to global digital elevation data and Schlumberger and IHS for granting educational software licenses for the interpretation of the seismic data. The German Ministry of Science and Education (BMBF) funded this study through the “Ritter Island project” grant [03G0252A].

8. Data Availability

The datasets analyzed in this study will be publicly available at the PANGAEA data repository (multibeam echosounder data: <https://doi.org/10.1594/PANGAEA.929026>, seismic data: <https://doi.org/10.1594/PANGAEA.929022>), once this article is published.

9. References

- Alves, T.M., Lourenço, S.D.N., 2010. Geomorphologic features related to gravitational collapse: Submarine landsliding to lateral spreading on a Late Miocene-Quaternary slope (SE Crete, eastern Mediterranean). *Geomorphology* 123, 13–33. <https://doi.org/10.1016/j.geomorph.2010.04.030>
- Baldwin, S.L., Fitzgerald, P.G., Webb, L.E., 2012. Tectonics of the New Guinea Region. *Annu. Rev. Earth Planet. Sci.* 40, 495–520. <https://doi.org/10.1146/annurev-earth-040809-152540>

695 Berndt, C., Klaucke, I., Kühn, M., 2021a. Multibeam bathymetry gridded data from SONNE
 696 cruise SO252. [https://doi.org/https://doi.org/10.1594/PANGAEA.929026](https://doi.org/10.1594/PANGAEA.929026)
 697 Berndt, C., Kühn, M., Karstens, J., 2021b. 2D multi-channel seismic data from SONNE cruise
 698 SO252 offshore Ritter Island, 2016, Bismarck Sea, Papua New Guinea.
 699 <https://doi.org/10.1594/PANGAEA.929022>
 700 Berndt, C., Muff, S., Klaucke, I., Watt, S., Böttner, C., Schramm, B., Völsch, A.-M.,
 701 Bennecke, S., Elger, J., Chi, W.-C., Van Haren, J., Micallef, A., Roth, T., 2016. RV
 702 SONNE 252 Cruise Report / Fahrtbericht Tsunami potential of volcanic flank collapses
 703 Table of content. https://doi.org/http://dx.doi.org/10.3289/CR_SO252
 704 Bjerrum, L., 1955. Stability of natural slopes in quick clay. *Géotechnique* 5, 101–119.
 705 [https://doi.org/https://doi.org/10.1680/geot.1955.5.1.101](https://doi.org/10.1680/geot.1955.5.1.101)
 706 Crutchley, G.J., Karstens, J., Berndt, C., Talling, P.J., Watt, S.F.L., Vardy, M.E., Hühnerbach,
 707 V., Urlaub, M., Sarkar, S., Klaeschen, D., Paulatto, M., Le Friant, A., Lebas, E., Maeno,
 708 F., 2013. Insights into the emplacement dynamics of volcanic landslides from high-
 709 resolution 3D seismic data acquired offshore Montserrat, Lesser Antilles. *Mar. Geol.*
 710 335, 1–15. <https://doi.org/10.1016/j.margeo.2012.10.004>
 711 Day, S., Llanes, P., Silver, E., Hoffmann, G., Ward, S., Driscoll, N., 2015. Submarine
 712 landslide deposits of the historical lateral collapse of Ritter Island, Papua New Guinea.
 713 *Mar. Pet. Geol.* 67, 419–438. <https://doi.org/10.1016/j.marpetgeo.2015.05.017>
 714 Day, S.J., Heleno Da Silva, S.I.N., Fonseca, J.F.B.D., 1999. A past giant lateral collapse and
 715 present-day flank instability of Fogo, Cape Verde Islands. *J. Volcanol. Geotherm. Res.*
 716 94, 191–218. [https://doi.org/10.1016/S0377-0273\(99\)00103-1](https://doi.org/10.1016/S0377-0273(99)00103-1)
 717 De Blasio, F.V., Elverhøi, A., Issler, D., Harbitz, C.B., Bryn, P., Lien, R., 2005. On the
 718 dynamics of subaqueous clay rich gravity mass flows - The giant Storegga slide,
 719 Norway. *Mar. Pet. Geol.* 22, 179–186. <https://doi.org/10.1016/j.marpetgeo.2004.10.014>
 720 Deplus, C., Le Friant, A., Boudon, G., Komorowski, J.C., Villemant, B., Harford, C.,

721 Ségoufin, J., Cheminée, J.L., 2001. Submarine evidence for large-scale debris avalanches
722 in the Lesser Antilles Arc. *Earth Planet. Sci. Lett.* 192, 145–157.
723 [https://doi.org/10.1016/S0012-821X\(01\)00444-7](https://doi.org/10.1016/S0012-821X(01)00444-7)

724 Frey-Martínez, J., Cartwright, J., James, D., 2006. Frontally confined versus frontally
725 emergent submarine landslides: A 3D seismic characterisation. *Mar. Pet. Geol.* 23, 585–
726 604. <https://doi.org/10.1016/j.marpetgeo.2006.04.002>

727 Gee, M.J.R., Uy, H.S., Warren, J., Morley, C.K., Lambiase, J.J., 2007. The Brunei slide: A
728 giant submarine landslide on the North West Borneo Margin revealed by 3D seismic
729 data. *Mar. Geol.* 246, 9–23. <https://doi.org/10.1016/j.margeo.2007.07.009>

730 Glicken, H., 1996. Rockslide-debris avalanche of may 18, 1980, Mount St. Helens volcano,
731 Washington. Open-file Rep. 96-677 1–5.

732 Gouhier, M., Paris, R., 2019. SO₂ and tephra emissions during the December 22, 2018 Anak
733 Krakatau flank-collapse eruption. *Volcanica* 2, 91–103.
734 <https://doi.org/10.30909/vol.02.02.91103>

735 Grilli, S.T., Tappin, D.R., Carey, S., Watt, S.F.L., Ward, S.N., Grilli, A.R., Engwell, S.L.,
736 Zhang, C., Kirby, J.T., Schambach, L., Muin, M., 2019. Modelling of the tsunami from
737 the December 22, 2018 lateral collapse of Anak Krakatau volcano in the Sunda Straits,
738 Indonesia. *Sci. Rep.* 9, 1–13. <https://doi.org/10.1038/s41598-019-48327-6>

739 Holm, R.J., Richards, S.W., 2013. A re-evaluation of arc-continent collision and along-arc
740 variation in the Bismarck Sea region, Papua New Guinea. *Aust. J. Earth Sci.* 60, 605–
741 619. <https://doi.org/10.1080/08120099.2013.824505>

742 Honza, E., Miyazaki, T., Lock, J., 1989. Subduction erosion and accretion in the Solomon Sea
743 region. *Tectonophysics* 160, 49–62. [https://doi.org/10.1016/0040-1951\(89\)90383-1](https://doi.org/10.1016/0040-1951(89)90383-1)

744 Hornbach, M.J., Manga, M., Genecov, M., Valdez, R., Miller, P., Saffer, D., Adelstein, E.,
745 Lafuerza, S., Adachi, T., Breitkreuz, C., Jutzeler, M., LeFriant, A., Ishizuka, O., Morgan,
746 S., Slagle, A., Talling, P.J., Fraass, A., Watt, S.F.L., Stroncik, N.A., Aljahdali, M.,

747 Boudon, G., Fujinawa, A., Hatfield, R., Kataoka, K., Maeno, F., Martinez-Colon, M.,
 748 McCanta, M., Palmer, M., Stinton, A., Subramanyam, K.S. V., Tamura, Y., Villemant,
 749 B., Wall-Palmer, D., Wang, and F., 2015. Permeability and pressure measurements in
 750 Lesser Antilles submarine slides: Evidence for pressure-driven slow-slip failure. *J.*
 751 *Geophys. Res. Solid Earth* 120, 7986–8011. <https://doi.org/10.1002/2015JB012061>
 752 Johnson, R., Kitts, S., Indies, W., Roobol, M.J., I, A.L.S., Wright, J. V, 1987. Large-scale
 753 volcanic cone collapse: the 1888 slope failure of Ritter volcano, and other examples from
 754 Papua New Guinea. *Bull. Volcanol.* 49, 669–679.
 755 Johnson, R.W., 1977. Distribution and major-element chemistry of late Cainozoic vol-
 756 canoes at the southern margin of the Bismarck Sea, PNG. *Aust. Bur. Miner. Resour. Geol.*
 757 *Geophys. Rep.* 188. 162 pp.
 758 Karstens, J., Berndt, C., Urlaub, M., Watt, S.F.L., Micallef, A., Ray, M., Klaucke, I., Muff, S.,
 759 Klaeschen, D., Kühn, M., Roth, T., Böttner, C., Schramm, B., Elger, J., Brune, S., 2019.
 760 From gradual spreading to catastrophic collapse – Reconstruction of the 1888 Ritter
 761 Island volcanic sector collapse from high-resolution 3D seismic data. *Earth Planet. Sci.*
 762 *Lett.* 517, 1–13. <https://doi.org/10.1016/j.epsl.2019.04.009>
 763 Karstens, J., Crutchley, G.J., Berndt, C., Talling, P.J., Watt, S.F.L., Hühnerbach, V., Friant,
 764 A. Le, Lebas, E., Trofimovs, J., 2013. Emplacement of pyroclastic deposits offshore
 765 Montserrat: Insights from 3D seismic data. *J. Volcanol. Geotherm. Res.* 257, 1–11.
 766 <https://doi.org/10.1016/j.jvolgeores.2013.03.004>
 767 Karstens, J., Kelfoun, K., Watt, S.F.L., Berndt, C., 2020. Combining 3D seismics, eyewitness
 768 accounts and numerical simulations to reconstruct the 1888 Ritter Island sector collapse
 769 and tsunami. *Int. J. Earth Sci.* <https://doi.org/10.1007/s00531-020-01854-4>
 770 Le Bas, T.P., Masson, D.G., Holtom, R.T., Grevemeyer, I., 2007. Slope failures of the flanks
 771 of the southern Cape Verde Islands. *Submar. Mass Movements Their Consequences*, 3rd
 772 *Int. Symp.* 337–345. https://doi.org/10.1007/978-1-4020-6512-5_35

773 Le Friant, A., 2015. Geochemistry, Geophysics, Geosystems. *Geochemistry Geophys.*
774 *Geosystems* 18, 1541–1576. <https://doi.org/10.1002/2014GC005684>.Key

775 Le Friant, A., Boudon, G., Deplus, C., Villemant, B., 2003. Large-scale flank collapse events
776 during the activity of Montagne Pelée, Martinique, Lesser Antilles. *J. Geophys. Res.*
777 *Solid Earth* 108, 1–15. <https://doi.org/10.1029/2001jb001624>

778 Lenz, B.L., Sawyer, D.E., Phrampus, B., Davenport, K., Long, A., 2019. Seismic imaging of
779 seafloor deformation induced by impact from large submarine landslide blocks, offshore
780 oregon. *Geosci.* 9. <https://doi.org/10.3390/geosciences9010010>

781 Løvholt, F., Harbitz, C.B., Haugen, K.B., 2005. A parametric study of tsunamis generated by
782 submarine slides in the Ormen Lange/Storegga area off western Norway. *Mar. Pet. Geol.*
783 22, 219–231. <https://doi.org/10.1016/j.marpetgeo.2004.10.017>

784 Løvholt, F., Pedersen, G., Harbitz, C.B., Glimsdal, S., Kim, J., 2015. On the characteristics of
785 landslide tsunamis. *Philos. Trans. R. Soc. A Math. Phys. Eng. Sci.* 373.
786 <https://doi.org/10.1098/rsta.2014.0376>

787 Mangeney, A., Roche, O., Hungr, O., Mangold, N., Faccanoni, G., Lucas, A., 2010. Erosion
788 and mobility in granular collapse over sloping beds. *J. Geophys. Res. Earth Surf.* 115, 1–
789 21. <https://doi.org/10.1029/2009JF001462>

790 Masson, D.G., Le Bas, T.P., Grevemeyer, I., Weinrebe, W., 2008. Flank collapse and large-
791 scale landsliding in the Cape Verde Islands, off West Africa. *Geochemistry, Geophys.*
792 *Geosystems* 9, 1–16. <https://doi.org/10.1029/2008GC001983>

793 Masson, D.G., Watts, A.B., Gee, M.J.R., Urgeles, R., Mitchell, N.C., Le Bas, T.P., Canals,
794 M., 2002. Slope failures on the flanks of the western Canary Islands. *Earth-Science Rev.*
795 57, 1–35. [https://doi.org/10.1016/S0012-8252\(01\)00069-1](https://doi.org/10.1016/S0012-8252(01)00069-1)

796 Mohrig, D., Whipple, K.X., Hondzo, M., Ellis, C., Parker, G., 1998. Hydroplaning of
797 subaqueous debris flows. *Bull. Geol. Soc. Am.* 110, 387–394.
798 [https://doi.org/10.1130/0016-7606\(1998\)110<0387:HOSDF>2.3.CO;2](https://doi.org/10.1130/0016-7606(1998)110<0387:HOSDF>2.3.CO;2)

799 Morita, S., Nakajima, T., Hanamura, Y., 2011. Submarine slump sediments and related
 800 dewatering structures: Observations of 3D seismic data obtained for the continental slope
 801 off Shimokita Peninsula, NE Japan. *J. Geol. Soc. Japan* 117, 95–98.
 802 <https://doi.org/10.5575/geosoc.117.95>

803 Mulder, T., Cochonat, P., 1996. Classification of offshore mass movements. *J. Sediment. Res.*
 804 66, 43–57.

805 Ogata, K., Festa, A., Pini, G.A., Pogačnik, Lucente, C.C., 2019. Substrate deformation and
 806 incorporation in sedimentary mélanges (olistostromes): Examples from the northern
 807 Apennines (Italy) and northwestern Dinarides (Slovenia). *Gondwana Res.* 74, 101–125.
 808 <https://doi.org/10.1016/j.gr.2019.03.001>

809 Ogata, K., Mountjoy, J.J., Pini, G.A., Festa, A., Tinterri, R., 2014a. Shear zone liquefaction in
 810 mass transport deposit emplacement: A multi-scale integration of seismic reflection and
 811 outcrop data. *Mar. Geol.* 356, 50–64. <https://doi.org/10.1016/j.margeo.2014.05.001>

812 Ogata, K., Mutti, E., Pini, G.A., Tinterri, R., 2012. Mass transport-related stratal disruption
 813 within sedimentary mélanges: Examples from the northern Apennines (Italy) and south-
 814 central Pyrenees (Spain). *Tectonophysics* 568–569, 185–199.
 815 <https://doi.org/10.1016/j.tecto.2011.08.021>

816 Ogata, K., Pogačnik, Z., Pini, G.A., Tunis, G., Festa, A., Camerlenghi, A., Rebesco, M.,
 817 2014b. The carbonate mass transport deposits of the Paleogene Friuli Basin
 818 (Italy/Slovenia): Internal anatomy and inferred genetic processes. *Mar. Geol.* 356, 88–
 819 110. <https://doi.org/10.1016/j.margeo.2014.06.014>

820 Pope, E.L., Jutzeler, M., Cartigny, M.J.B., Shreeve, J., Talling, P.J., Wright, I.C.,
 821 Wysoczanski, R.J., 2018. Origin of spectacular fields of submarine sediment waves
 822 around volcanic islands. *Earth Planet. Sci. Lett.* 493, 12–24.
 823 <https://doi.org/10.1016/j.epsl.2018.04.020>

824 Quinn, P.E., Diederichs, M.S., Rowe, R.K., Hutchinson, D.J., 2012. Development of

825 progressive failure in sensitive clay slopes. *Can. Geotech. J.* 49, 782–795.

826 <https://doi.org/10.1139/T2012-034>

827 Siebert, L., 1984. Large volcanic debris avalanches: Characteristics of source areas, deposits,
828 and associated eruptions. *J. Volcanol. Geotherm. Res.* 22, 163–197.

829 [https://doi.org/10.1016/0377-0273\(84\)90002-7](https://doi.org/10.1016/0377-0273(84)90002-7)

830 Siebert, L., Roverato, M., 2021. A Historical Perspective on Lateral Collapse and Volcanic
831 Debris Avalanches, in: Roverato, M., Dufresne, A., Procter, J. (Eds.), *Volcanic Debris*
832 *Avalanches: From Collapse to Hazard*. Springer International Publishing, Cham, pp. 11–
833 50. https://doi.org/10.1007/978-3-030-57411-6_2

834 Silver, E., Day, S., Ward, S., Hoffmann, G., Llanes, P., Driscoll, N., Appelgate, B., Saunders,
835 S., 2009. Volcano collapse and tsunami generation in the Bismarck Volcanic Arc, Papua
836 New Guinea. *J. Volcanol. Geotherm. Res.* 186, 210–222.

837 <https://doi.org/10.1016/j.jvolgeores.2009.06.013>

838 Sobiesiak, M.S., Kneller, B., Alsop, G.I., Milana, J.P., 2018. Styles of basal interaction
839 beneath mass transport deposits. *Mar. Pet. Geol.* 98, 629–639.

840 <https://doi.org/10.1016/j.marpetgeo.2018.08.028>

841 Taylor, B., 1979. Bismarck Sea: Evolution of a back-arc basin. *Geology* 7, 171–174.

842 [https://doi.org/10.1130/0091-7613\(1979\)7<171:BSEOAB>2.0.CO;2](https://doi.org/10.1130/0091-7613(1979)7<171:BSEOAB>2.0.CO;2)

843 Urlaub, M., Petersen, F., Gross, F., Bonforte, A., Puglisi, G., Guglielmino, F., Krastel, S.,
844 Lange, D., Kopp, H., 2018. Gravitational collapse of Mount Etna’s southeastern flank.
845 *Sci. Adv.* 4, 1–8. <https://doi.org/10.1126/sciadv.aat9700>

846 Van Der Merwe, W.C., Hodgson, D.M., Flint, S.S., 2011. Origin and terminal architecture of
847 a submarine slide: A case study from the Permian Vischkui Formation, Karoo Basin,
848 South Africa. *Sedimentology* 58, 2012–2038. [https://doi.org/10.1111/j.1365-](https://doi.org/10.1111/j.1365-3091.2011.01249.x)
849 [3091.2011.01249.x](https://doi.org/10.1111/j.1365-3091.2011.01249.x)

850 Walter, T.R., Haghshenas Haghighi, M., Schneider, F.M., Coppola, D., Motagh, M., Saul, J.,

851 Babeyko, A., Dahm, T., Troll, V.R., Tilmann, F., Heimann, S., Valade, S., Triyono, R.,
 852 Khomarudin, R., Kartadinata, N., Laiolo, M., Massimetti, F., Gaebler, P., 2019. Complex
 853 hazard cascade culminating in the Anak Krakatau sector collapse. *Nat. Commun.* 10.
 854 <https://doi.org/10.1038/s41467-019-12284-5>
 855 Ward, S.N., Day, S., 2003. Ritter Island Volcano - Lateral collapse and the tsunami of 1888.
 856 *Geophys. J. Int.* 154, 891–902. <https://doi.org/10.1046/j.1365-246X.2003.02016.x>
 857 Watt, S.F.L., Karstens, J., Berndt, C., 2021. Volcanic-Island Lateral Collapses and Their
 858 Submarine Deposits, *Advances in Volcanology*. Springer International Publishing.
 859 https://doi.org/10.1007/978-3-030-57411-6_10
 860 Watt, S.F.L., Karstens, J., Micallef, A., Berndt, C., Urlaub, M., Ray, M., Desai, A.,
 861 Sammartini, M., Klaucke, I., Böttner, C., Day, S., Downes, H., Kühn, M., Elger, J., 2019.
 862 From catastrophic collapse to multi-phase deposition: Flow transformation, seafloor
 863 interaction and triggered eruption following a volcanic-island landslide. *Earth Planet.*
 864 *Sci. Lett.* 517, 135–147. <https://doi.org/10.1016/j.epsl.2019.04.024>
 865 Watt, S.F.L., Talling, P.J., Vardy, M.E., Heller, V., Hühnerbach, V., Urlaub, M., Sarkar, S.,
 866 Masson, D.G., Henstock, T.J., Minshull, T.A., Paulatto, M., Le Friant, A., Lebas, E.,
 867 Berndt, C., Crutchley, G.J., Karstens, J., Stinton, A.J., Maeno, F., 2012a. Combinations
 868 of volcanic-flank and seafloor-sediment failure offshore Montserrat, and their
 869 implications for tsunami generation. *Earth Planet. Sci. Lett.* 319–320, 228–240.
 870 <https://doi.org/10.1016/j.epsl.2011.11.032>
 871 Watt, S.F.L., Talling, P.J., Vardy, M.E., Masson, D.G., Henstock, T.J., Hühnerbach, V.,
 872 Minshull, T.A., Urlaub, M., Lebas, E., Le Friant, A., Berndt, C., Crutchley, G.J.,
 873 Karstens, J., 2012b. Widespread and progressive seafloor-sediment failure following
 874 volcanic debris avalanche emplacement: Landslide dynamics and timing offshore
 875 Montserrat, Lesser Antilles. *Mar. Geol.* 323–325, 69–94.
 876 <https://doi.org/10.1016/j.margeo.2012.08.002>

877 Weiß, B.J., Hübscher, C., Wolf, D., Lüdmann, T., 2015. Submarine explosive volcanism in
 878 the southeastern Terceira Rift/São Miguel region (Azores). *J. Volcanol. Geotherm. Res.*
 879 303, 79–91. <https://doi.org/10.1016/j.jvolgeores.2015.07.028>
 880 Woodhead, J., Hergt, J., Sandiford, M., Johnson, W., 2010. The big crunch: Physical and
 881 chemical expressions of arc/continent collision in the Western Bismarck arc. *J. Volcanol.*
 882 *Geotherm. Res.* 190, 11–24. <https://doi.org/10.1016/j.jvolgeores.2009.03.003>
 883 Yoshida, H., Sugai, T., Ohmori, H., 2012. Geomorphology Size – distance relationships for
 884 hummocks on volcanic rockslide-debris avalanche deposits in Japan. *Geomorphology*
 885 136, 76–87. <https://doi.org/10.1016/j.geomorph.2011.04.044>
 886

147° 40' E WGS84 147° 50' E 148° 00' E 148° 10' E

4° 50' S

5° 00' S

5° 10' S

5° 20' S

5° 30' S

5° 40' S

transition of internally chaotic sub-facies
to deformed sediment sub-facies within SLD2

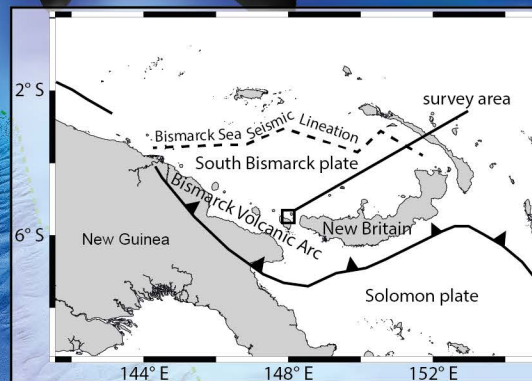
valley- or channel-like
morphology

valley- or channel-like
morphology

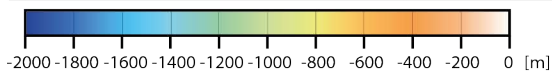
Sakar

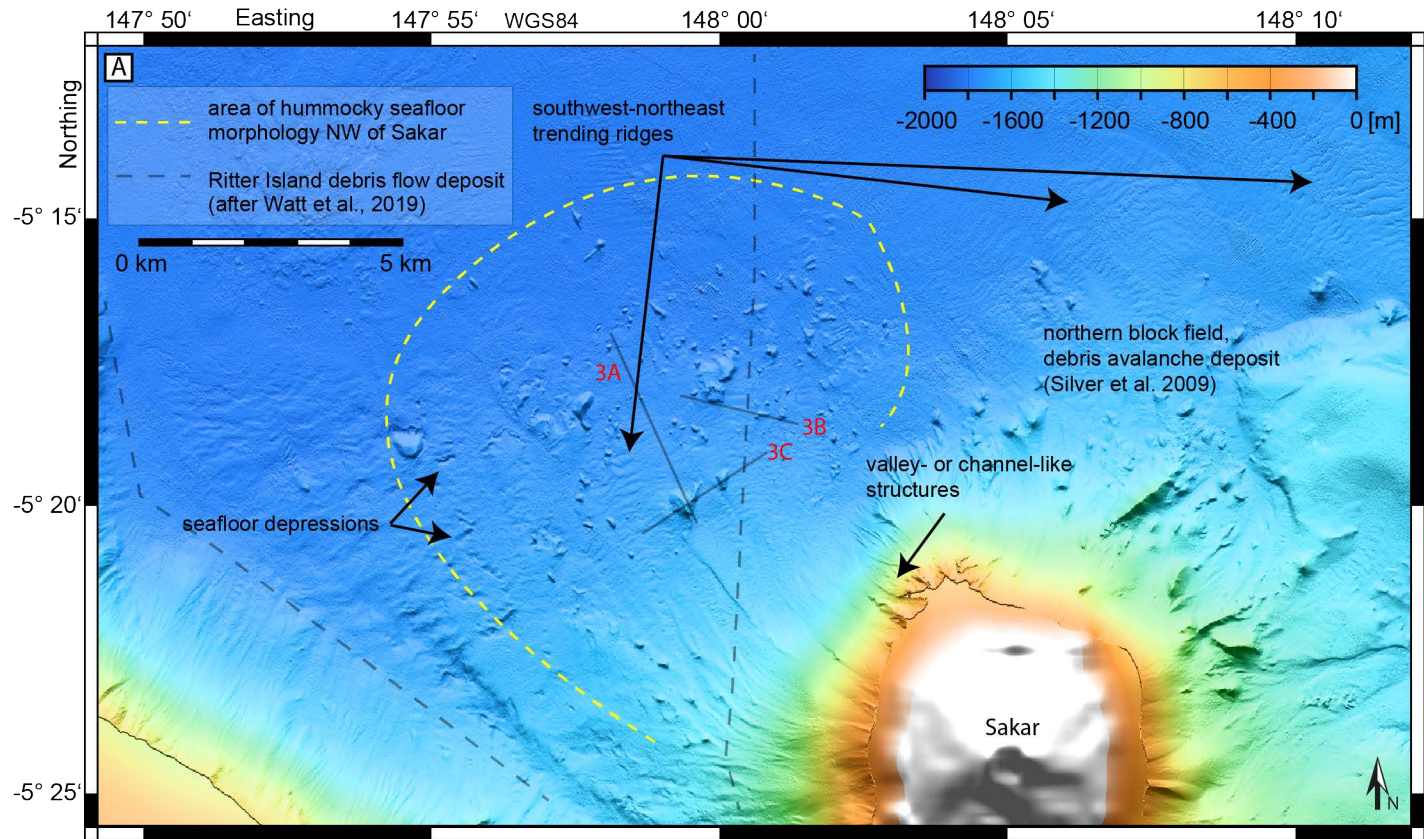
Ritter

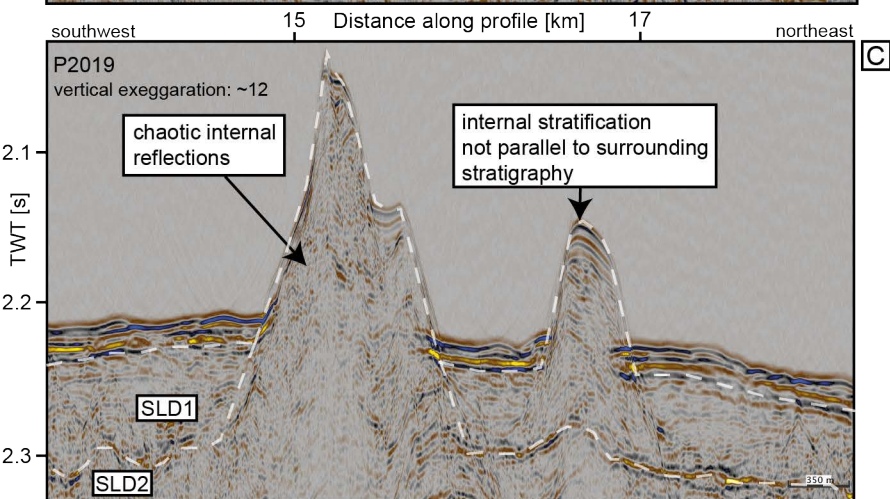
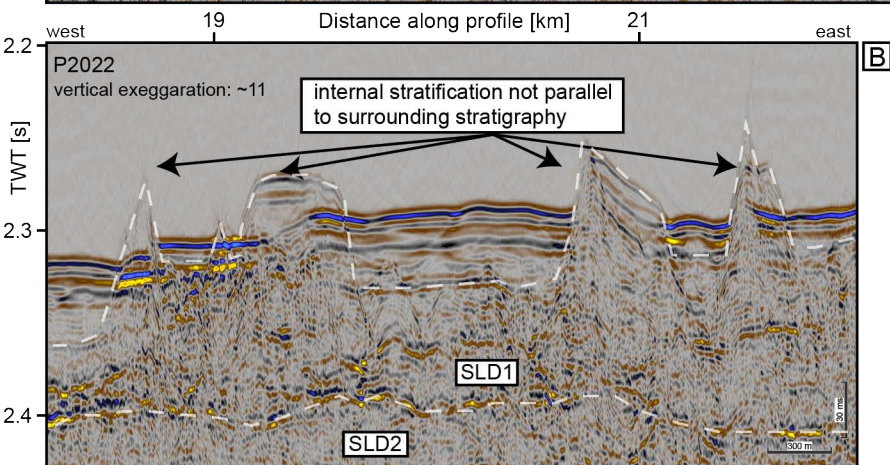
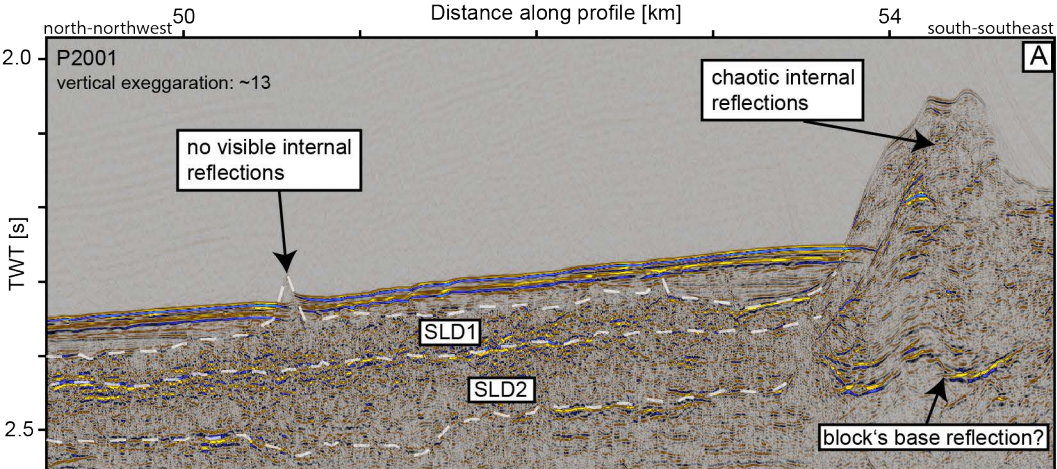
Umboi

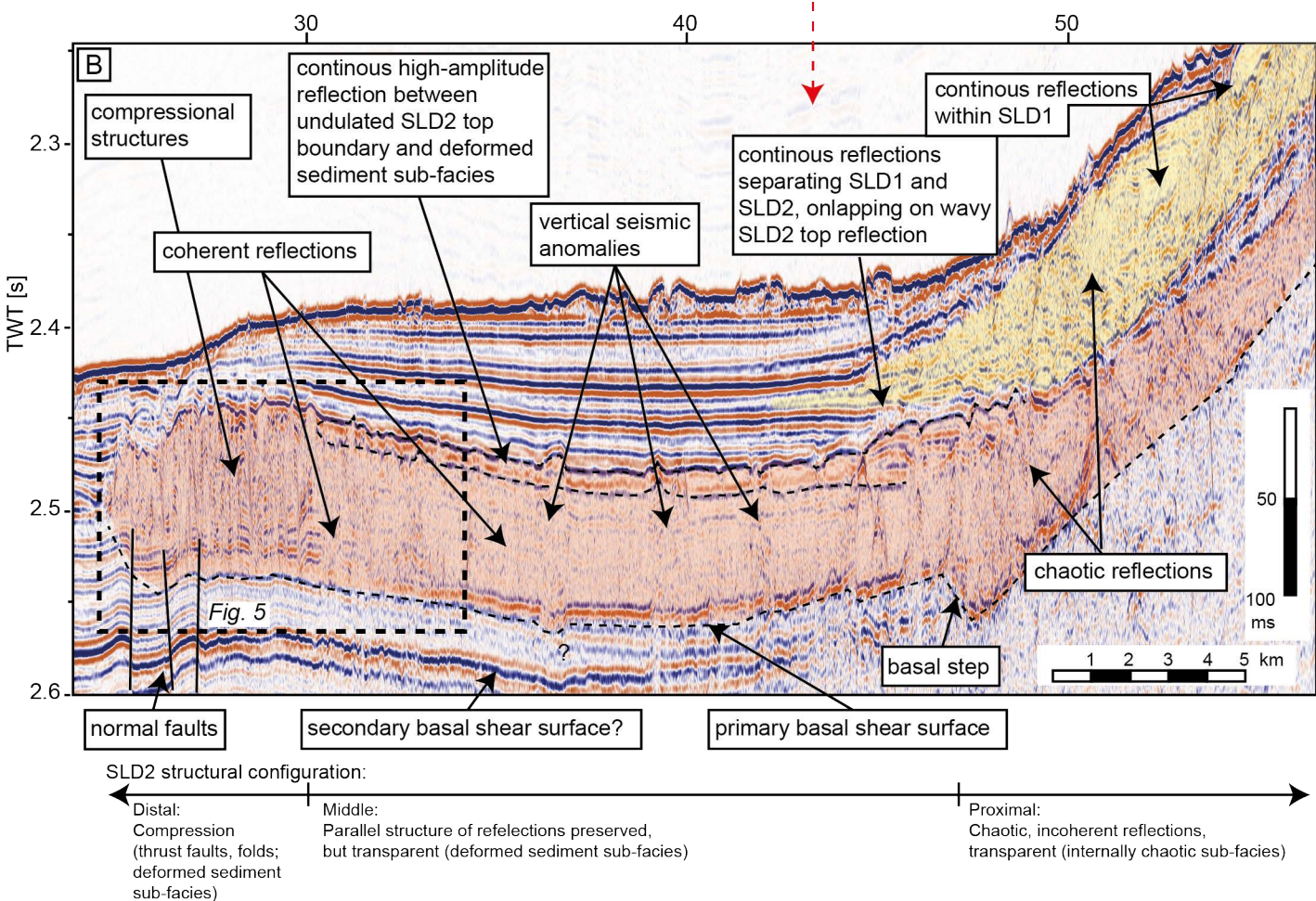
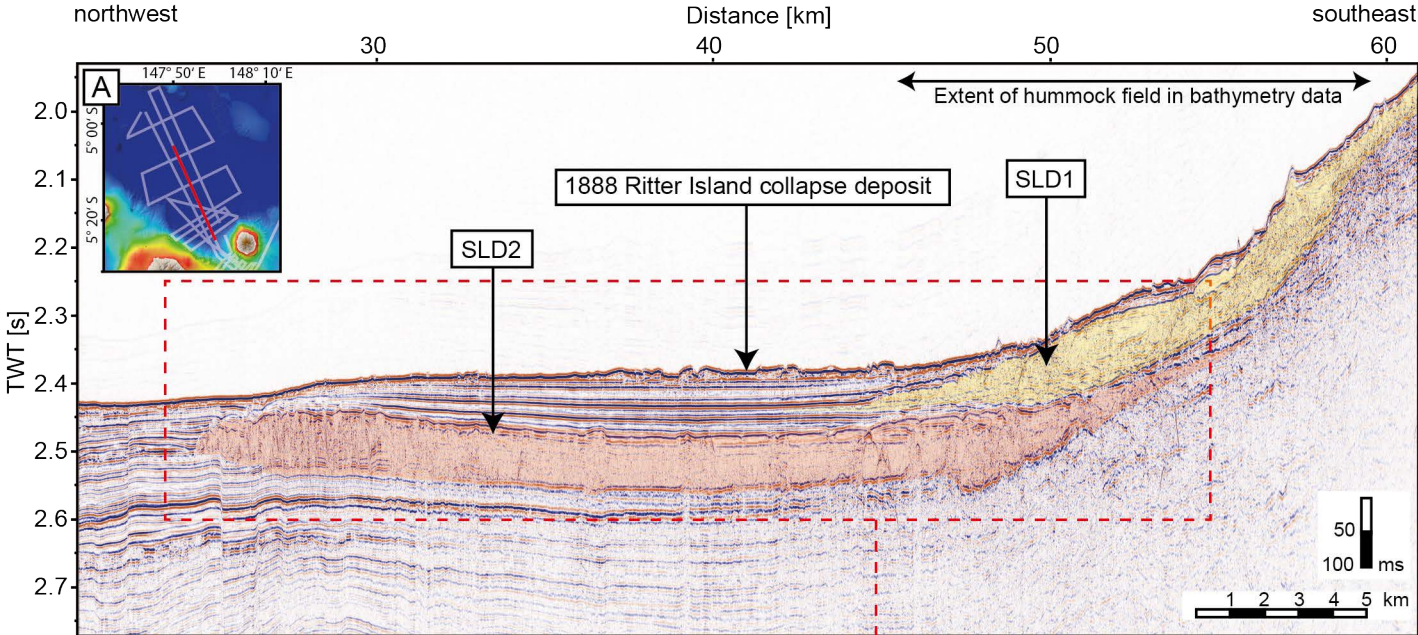


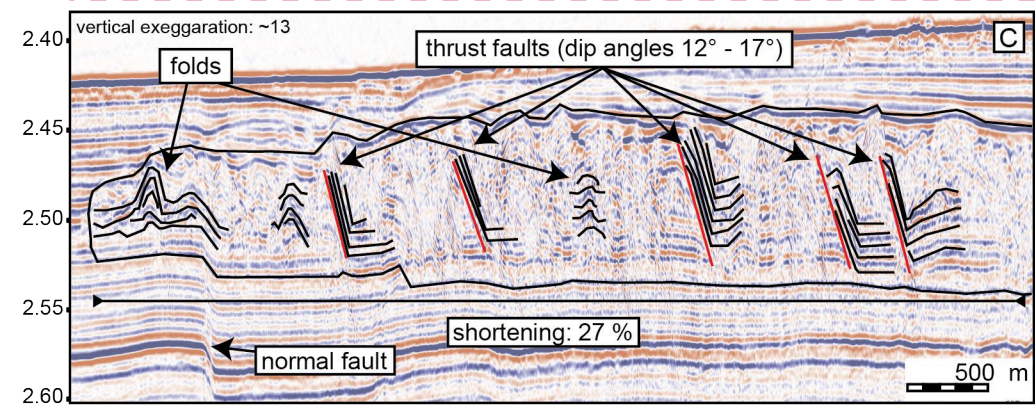
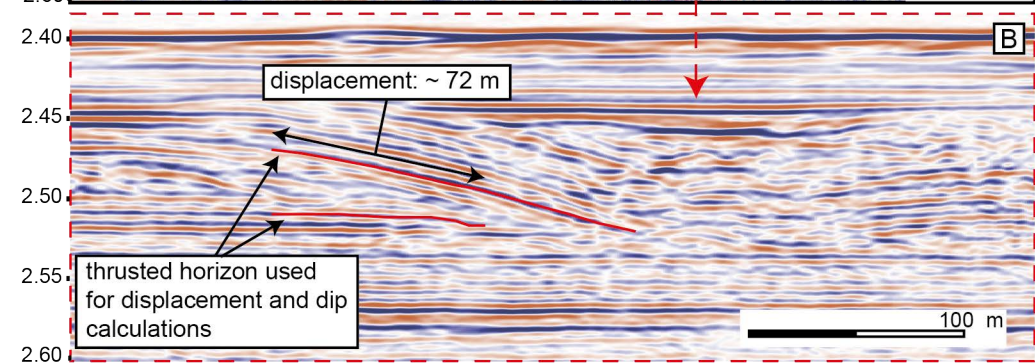
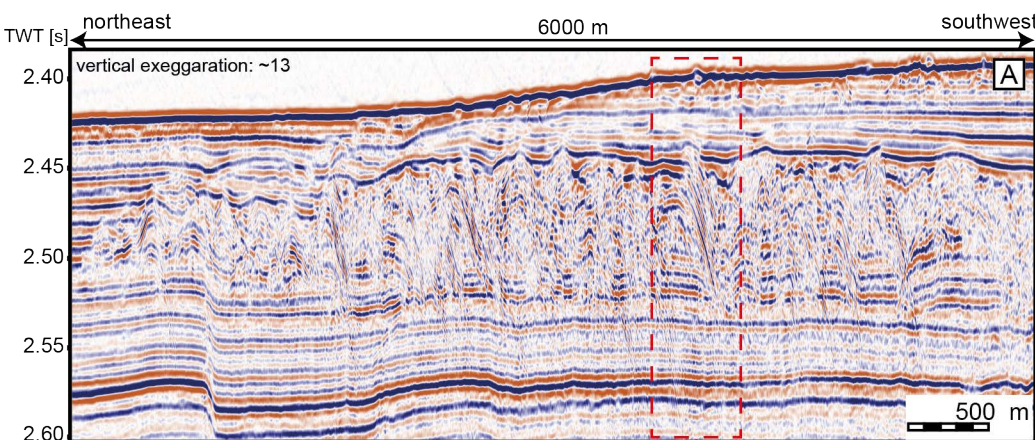
- extent SLD1
- extent SLD2
- SO252 2D MCS Profiles
- - - transition high-res.
Bathymetry / GEBCO





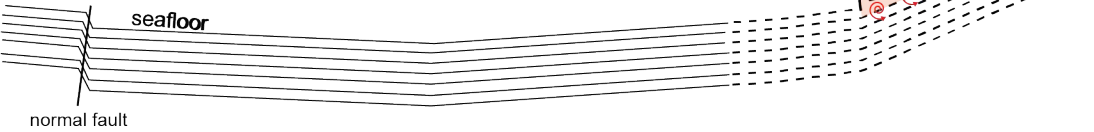






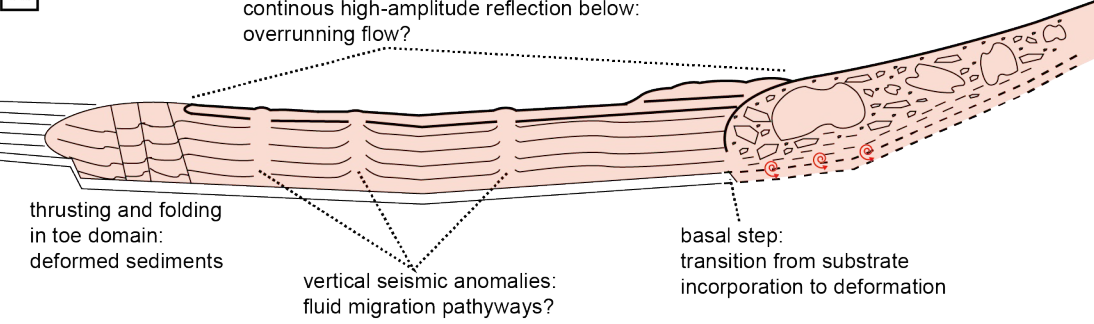
A

substrate incorporation
by downslope travelling
debris avalanche from Sakar



B

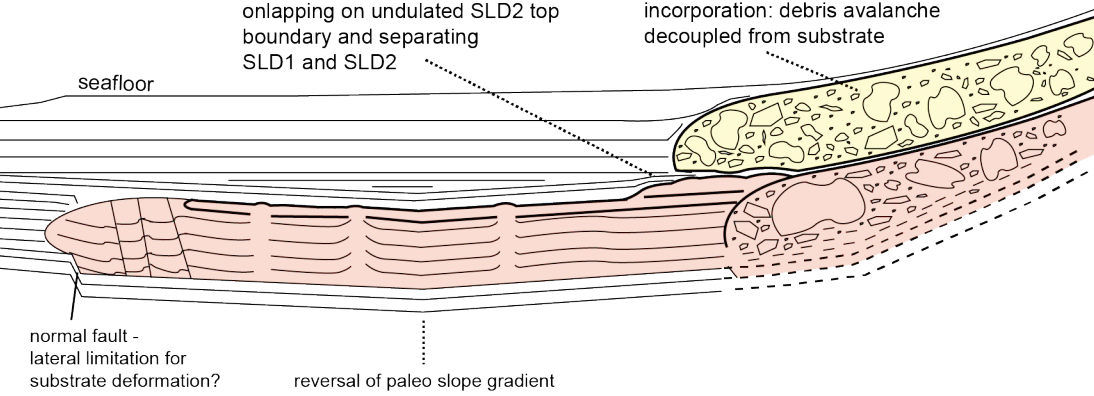
undulated top boundary of SLD2 &
continous high-amplitude reflection below:
overrunning flow?



C

well-bedded sediment facies
onlapping on undulated SLD2 top
boundary and separating
SLD1 and SLD2

SLD1 deposited above SLD2
without imageable substrate (SLD2)
incorporation: debris avalanche
decoupled from substrate



SLD2 substrate interaction: substrate deformation

substrate incorporation



SLD1



SLD2

Figure 1: Map of the study region, showing the extents of SLD1 and SLD2 (dashed line indicates the limits of clear deposit imaging). The solid black lines mark acquired 2D multichannel seismic profiles (Karstens et al., 2019; Watt et al., 2019). Background: High-resolution bathymetry acquired during SO252 merged with low-resolution GEBCO grid (transition at dotted green line). Right corner: Overview map showing the general tectonic setting of the area.

Figure 2: A: Bathymetry of the hummock field northwest of Sakar. The dashed yellow line marks the extent of the hummock field, broadly coinciding with the margin of SLD1 in seismic reflection profiles. The dashed grey lines mark the margins of the 1888 Ritter Island collapse deposit, after Watt et al. (2019). Grey lines mark the locations of the seismic sections shown in Fig. 3A, 3B and 3C.

Figure 3: Selected seismic-reflection profiles through SLD1 and SLD2 (locations on Fig. 2). A: Profile across a ~900 m wide hummock with chaotic internal stratification (right) and a hummock with no visible internal reflections (left). The large hummock appears to be rooted within SLD2. B: Profile showing four hummocks apparently rooted within SLD1, which are either seismically transparent (low amplitude) or have stratigraphically chaotic internal structures or stratification that is not parallel to the surrounding stratigraphy. C: Profile showing the 900-m-wide hummock from A in an orthogonal direction and another, smaller hummock with stratification not parallel to the surroundings. In all panels, dashed lines indicate the top and bottom boundaries of SLD1 and SLD2.

Figure 4: Northwest-southeast oriented seismic section showing SLD1 and SLD2 with annotated interpretations. A: Extent of SLD1, SLD2 and the 1888 Ritter Island collapse deposit (see inset map). B: Detail of the internal architecture of SLD1 and SLD2.

Figure 5: A: Profile through the distal section of SLD2, revealing compressional structures including thrust faults and folds, over ~5 km. B: Detail of a thrust fault without vertical exaggeration. C: Interpreted version of Panel A, showing horizons used to constrain the minimum magnitude of shortening.

Figure 6: Model for the emplacement of SLD1 and SLD2. A: A blocky debris avalanche associated with SLD2 flowing downslope, starting to incorporate and incise into the substrate. Different specific incorporation mechanisms are discussed in the text. B: The situation after the emplacement of SLD2, showing substrate incorporation (right) and frontal, downslope deformation, driven by impact and augmented by an overrunning flow, derived from the initial debris avalanche. The distal deformation limit is associated with a pre-existing fault, disrupting the stratigraphy, and a reversal in the paleo-basin slope gradient. C: The situation before the Ritter Island 1888 landslide deposit, showing the blocky debris avalanche of SLD1, emplaced above SLD2 without incorporating the substrate (SLD2 and the relatively thin intervening sediment package), indicating a decoupling of the slide mass from the substrate. Both landslides have been subsequently buried by younger basin infill.